Measuring the Wind Vector Using the Autonomous Mini Aerial Vehicle M^{2}AV

ALINE VAN DEN KROONENBERG AND TIM MARTIN

Institute of Aerospace Systems, Technical University of Braunschweig, Braunschweig, Germany

MARCO BUSCHMANN

Mavionics GmbH, Braunschweig, Germany

JENS BANGE AND PETER VÖRSMANN

Institute of Aerospace Systems, Technical University of Braunschweig, Braunschweig, Germany

(Manuscript received 22 January 2008, in final form 11 April 2008)

ABSTRACT

The meteorological mini unmanned aerial vehicle (M^{2}AV) was used for measuring the meteorological wind. The wind is the vector difference between the aircraft speed relative to the earth (inertial velocity) and relative to the airflow (true airspeed). The latter was computed from five-hole-probe pressure measurements in combination with calibration–coefficient polynomials obtained during wind tunnel calibration. The aircraft inertial velocity, position, and attitude were calculated using a Kalman filter that combined data from a global positioning system (GPS) and an inertial navigation system (INS). The temporal (and spatial) resolution of the M^{2}AV wind measurement is remarkably fine. An inertial subrange of locally isotropic turbulence can be measured up to 40 Hz (or 0.55 m at 22 m s^{-1} airspeed).

The first M^{2}AV wind estimation showed some systematic deviations compared to the expected values (like a constant mean wind in every flight direction). Therefore, an in-flight wind calibration technique was developed that corrects for the inaccuracy of the true heading, the constant offset of the pitch angle, and the underestimation of the true airspeed. The final adjusted wind measurements were verified during a field experiment at the measurement field of the German Meteorological Service, southeast of Berlin. The mean horizontal and vertical wind measured by the M^{2}AV agreed well with simultaneous sodar and tower measurements.

1. Introduction

Aircraft measurements play an important role in boundary layer research. The main advantage of airborne systems is their flexibility: they are capable of measuring on horizontal tracks or probing the boundary layer vertically by slant profiles. Because of its high operational speed, an aircraft can obtain statistically significant measurements faster than ground-based measurement systems. Research aircraft are therefore involved in large field experiments in addition to ground stations and remote sensing systems with area-representative measurements (e.g., Bange et al. 2002; Beyrich and Mengelkamp 2006). An important variable for boundary layer research is the wind vector. The wind vector calculation from airborne measurements is complex and described by many authors, mostly based on the studies of Axford (1968) and Lenschow (1986). The difference between the aircraft velocity relative to the earth (inertial velocity) and the velocity relative to the air (true airspeed) results in the wind vector. The wind vector is small compared to the true airspeed and the inertial velocity vectors and is subject to the errors of the complex determination of these vectors (Grossman 1977). The attitude, velocity, and position of an aircraft constitutes a dynamic system whose state can be estimated by a Kalman filter. Error-state Kalman filters were previously applied by Leach and MacPherson (1991) to improve the accuracy of wind components. In recent decades, navigation technology has improved [e.g., the advent of the global positioning system (GPS)], which has resulted in more accurate turbulent flux and wind measurements by airborne systems (e.g.,

Corresponding author address: Aline van den Kroonenberg, Institut fur Luft- und Raumfahrtsysteme, TU Braunschweig, 38108 Braunschweig, Germany.
E-mail: a.kroonenberg@tu-bs.de

DOI: 10.1175/2008JTECHA1114.1

Brown et al. 1983; Crawford and Dobosy 1992; Scott et al. 1990; Tjernström and Friehe 1991; Wood et al. 1997; Khelif et al. 1999).

During the last ten years, a new trend in airborne meteorology has evolved: the operation of mini unmanned aerial vehicles (UAVs). The mini UAVs are inexpensive compared to a fully equipped research aircraft and are highly flexible. Some manual radio-controlled UAVs are already successfully in operation, measuring temperature and humidity (Egger et al. 2002; Hobbs et al. 2002). The disadvantage of radio-controlled systems is the limited measurement range. The systems must remain within sight, which reduces the range to 600–700 m in the horizontal and even less in the vertical distance. To expand the measurement range, an autopilot on board is necessary. Since 1997, the robotic plane meteorological sounding system (RPMSS) developed by the Chinese Meteorological Administration in Beijing has participated in several field campaigns (Ma et al. 2004). The RPMSS has a wingspan of 3 m and a take-off weight of about 13 kg, and the engine is powered by gasoline, which results in a flight endurance between 4 and 8 h. The system is used for soundings up to a height of 5 km, measuring the temperature, humidity, and wind vector. The wind vector is derived by the displacement of the RPMSS during spiral flight trajectory (comparable to wind measurements with balloons). The Aerosonde is another autonomous UAV which has operated in field experiments since 1998 (Holland et al. 2001; Soddell et al. 2004). This long-range UAV was developed in Australia and is now produced by Aerosonde North America. The Aerosonde has a wingspan of 3 m and a take-off weight between 12 and 14 kg. During flight the system is under control of an on-board autopilot, and the flight missions can be changed by uploading new way points to the aircraft during flight. Among other values, the Aerosonde measures the temperature, relative humidity, and the wind vector. The horizontal wind is calculated using GPS groundspeed (the horizontal component of inertial velocity) and the airspeed from a pitot tube mounted on the nose. Because only scalar wind speed is available (no airflow angles), the wind can only be calculated by performing special flight maneuvers; this wind-finding method provides a horizontal resolution of about 300 m.

The meteorological mini UAV (M^2AV) was developed at the Institute of Aerospace Systems (i.e., the Institut für Luft- und Raumfahrtsysteme, or ILR) at the Technical University of Braunschweig and build in cooperation with Mavionics GmbH, Braunschweig, Germany. The M^2AV, Fig 1, is a twin-engine (electric propulsion) aircraft with a wingspan of 2 m and a maximum take-off weight of 6 kg. The M^2AV is controlled by an onboard autopilot system. The meteorological sensor package consists of two temperature sensors, a humidity sensor, and a five-hole probe (5HP). A GPS receiver and an inertial measurement unit (IMU) are on board to measure the inertial velocity and the attitude angles. A Kalman filter is used to couple GPS and an inertial navigation system (INS; Winkler and Vörsmann 2007). Combined with the measurement data from the 5HP, the M^2AV is capable of calculating the mean and the turbulent wind vector with 40-Hz resolution, corresponding to a spatial resolution of 55 cm. The first meteorological performance was during the LAUNCH-05 field experiment (October 2005) at the Meteorological Observatory Lindenberg (MOL) of the German Meteorological Service (i.e., Deutscher Wetterdienst or DWD) (Spieß et al. 2007). Furthermore, three M^2AV systems operated successfully during a 14-month stay (October 2007–December 2008) at Halley Station, Antarctica, for the British Antarctic Survey.

FIG. 1. The M^2AV system.

In this paper we will focus on how the wind vector is calculated. This includes the 5HP calibration, the description of the INS–GPS fusion using the Kalman filter, the error estimation, and an in-flight wind calibration. In the second part, wind measurements are presented from a small field experiment at the MOL site of the DWD.

2. M^2AV instrumentation

The aircraft can be hand-launched or started with a bungee rope. After the takeoff, the way-point navigation is activated and the system flies autonomously. A laptop computer is used to follow the aircraft's mission and to check some (meteorological) parameters which are sent from the aircraft to the laptop using a radio link. Within the radio link, the mission can be changed

TABLE 1. Specification and performance of the M^{2}AV.

Takeoff weight	6 kg
Wing span	2 m
Twin engine	Electric propulsion
Navigation	GPS, IMU
Optimal speed	21–24 m s^{-1}
Max climbing rate	5 m s^{-1}
Endurance	<60 min
Horizontal distance	60–70 km
Altitude range	10–800 m AGL

by sending new way-points to the aircraft. Outside of the radio link range, the aircraft continues the commanded mission and can reach a flight distance of 60–70 km (at an airspeed of 22 m s^{-1}). The landing procedure can be done automatically or manually. The detailed specifications were published by Buschmann et al. (2004) and Spieß et al. (2007); a summary is listed in Table 1.

a. Autopilot system

The flight-guidance algorithm developed for the M^{2}AV uses user-defined cubic splines to determine the flight trajectory. This ensures deterministic curve radii between spline segments and allows for an easy definition of complex flight patterns. At test flights under moderate to harsh conditions (10 m s^{-1} mean wind speed, with gusts up to 12 m s^{-1}), the new spline trajectory controller was able to minimize the distance from the aircraft to the planned trajectory to better than 5 m vertically and 10 m horizontally at any time. On straight legs under less severe conditions, the difference between commanded and actual altitudes was smaller than ±1 m and the lateral deviation was less than ±2 m.

b. Meteorological sensor package

The meteorological package consists of one fast temperature sensor (thin foil element) developed by Dantec and a Vaisala Intercap (HMP50), which measures the temperature and relative humidity with a response time (in flight) of 1 s. A 5HP manufactured by the Institute of Fluid Dynamics (TU Braunschweig) measures five differential pressures at the tip of the probe (Fig. 2). The static pressure is measured by four holes at the side of the probe. The measurements are used to calculate the airflow angles and the dynamic pressure (see following paragraph). A microelectromechanical sensor system (MEMS) gives time series of the angle accelerations and the accelerations in the x, y, and z directions and was developed at the ILR. The sensor

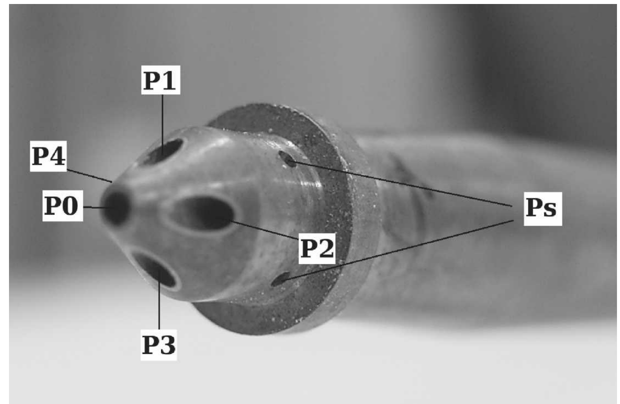

FIG. 2. The 5HP with a diameter of 6 mm. At the tip, the central hole P_0 is visible. Around the central hole, two holes are positioned in the vertical, (upper) P_1, and (lower) P_3 and two holes are positioned in the horizontal, (left) P_4, and (right) P_2. The four smaller circumferential holes (only two are visible) are the static pressure ports.

block contains a three-axis IMU, which consists of three angular-rate sensors with a range of ±300° s^{-1} and two accelerometers with two axes each, providing redundancy for the aircraft's longitudinal axis (for specifications, see Table 2). The range is 2 times the force of gravity (g) for the horizontal and 10 g for the vertical axis. The IMU has a weight of less than 15 g and a size of 40 × 40 × 16 mm^3. The IMU was calibrated for the determination of the scale factor (sensor sensitivity), bias, and misalignment (Buschmann et al. 2006). The temperature influence on calibration data was not explicitly taken into account. Because of the integration with GPS, changes in sensor bias can be estimated by the navigation filter and extracted from the measurements. Surface and flight tests have shown biases of 0.1–0.15 m s^{-2} and 0.6–2.3° s^{-1}. The inertial velocity vector and the position are measured by a single-antenna single-frequency GPS receiver (μ-blox company, type SAM LS) with a measurement frequency of 1 Hz. Except for the GPS receiver, the IMU and the meteorological sensors are sampled with 100 Hz.

3. Wind vector

Wind measurement by airborne systems is challenging. High resolution and thus fast and accurate sensors

TABLE 2. Properties of the MEMS IMU.

Sensor	Noise	Resolution
Accelerometer (horizontal axis)	0.13 m s^{-1} h$^{1/2}$	0.012 m s^{-2}
Accelerometer (vertical axis)	0.37 m s^{-1} h$^{1/2}$	0.035 m s^{-2}
Angular rates (gyro)	1.82° h$^{-1/2}$	0.24° s^{-1}

are needed to determine the attitude, position, and velocity of the aircraft relative to the earth, as well as the airflow at the nose of the fuselage, with high accuracy.

The wind vector $\mathbf{W}_g$ defined in geodetic coordinate system is the vector difference between the inertial velocity vector $\mathbf{V}_g$ and the true airspeed U_a (neglecting the small lever-arm to the 5HP):

$$\mathbf{W}_g = \mathbf{V}_g + \mathbf{M}_{gb}\mathbf{M}_{ba}\mathbf{U}_a, \tag{1}$$

with the matrix $\mathbf{M}_{ba}$ to transform the true airspeed from aerodynamic (index a) to body (index b) coordinates, and $\mathbf{M}_{gb}$ for the transformation into the geodetic coordinate system (index g). An overview of the three coordinate systems of the airplane is shown in Fig. 3.

To obtain all components of (1) in the geodetic coordinate system, two coordinate transformations have to be applied. First, the true airspeed vector $\mathbf{U}_a$ as measured in the aerodynamic coordinate system has to be transformed into the body coordinate system of the aircraft using the transformation according to Boiffier (1998), Lenschow (1986), and Axford (1968):

$$\mathbf{U}_b = \mathbf{M}_{ba}\mathbf{U}_a = \frac{|\mathbf{U}_a|}{D}\begin{bmatrix} 1 \\ \tan\beta \\ \tan\alpha \end{bmatrix}, \tag{2}$$

with a normalization factor

$$D = \sqrt{1 + \tan^2\alpha + \tan^2\beta} \tag{3}$$

and the angles α, β (measured by the 5HP in flight) between the airflow and the x and z axes, respectively, in the body coordinate system. The norm $|\mathbf{U}_a|$ has to be calculated using the measured total air temperature T_{tot}, the static pressure p and the dynamic pressure q:

$$|\mathbf{U}_a|^2 = 2c_pT_{\text{tot}}\left[1 - \left(\frac{p}{p+q}\right)^{\kappa}\right], \tag{4}$$

with the Poisson number $\kappa = R/c_p$, where $R = 287$ J K^{-1} kg^{-1} is the gas constant for dry air and $c_p = 1005$ J kg^{-1} K^{-1} is the specific heat for dry air.

Then, the flow vector $\mathbf{U}_b$ has to be transformed into the geodetic, Fig. 3 system using $\mathbf{M}_{gb}$ (Haering 1990; Leise and Masters 1993; Boiffier 1998). Finally, the resulting $\mathbf{W}_g$ has to be transformed into the standard meteorological frame of reference, with the wind components u, v, and w (east-, north-, and upward, respectively; Lenschow 1986):

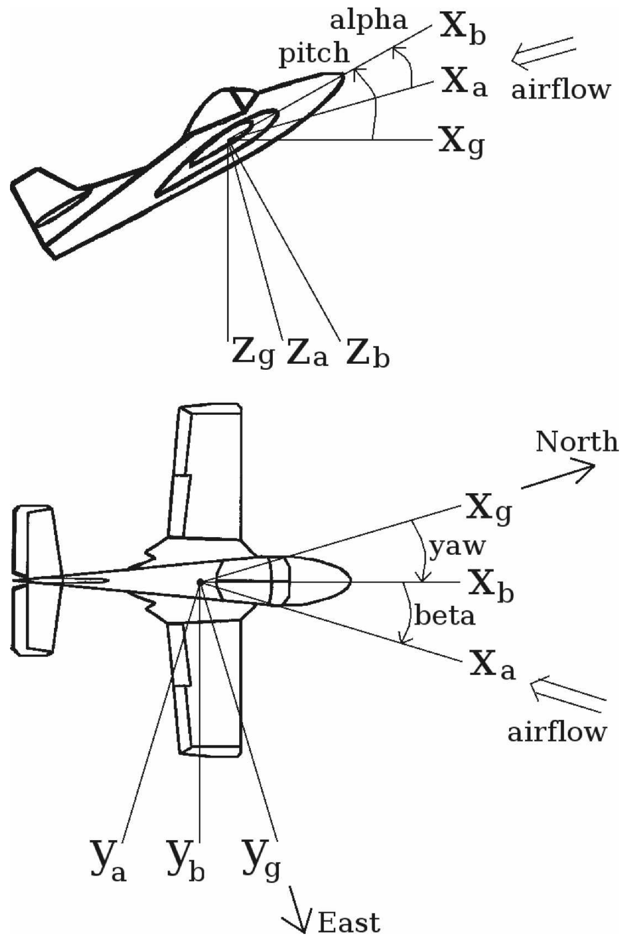

FIG. 3. The three coordinate systems used to transform the true airspeed into the geodetic coordinate system. The indices a, b, and g represent, respectively, the aerodynamic, body, and geodetic coordinate systems. "Alpha" is the angle of attack α, "beta" the sideslip angle β, "yaw" the true heading Ψ, and "pitch" the pitch angle Θ.

$$\begin{aligned}
u = v_g = v_{Ag} - |\mathbf{U}_a|D^{-1}[&(\cos\Theta\,\sin\Psi) + \tan\beta(\sin\Phi\,\sin\Theta\,\sin\Psi + \cos\Phi\,\cos\Psi) \\
&+ \tan\alpha(\cos\Phi\,\sin\Theta\,\sin\Psi - \sin\Phi\,\cos\Psi)],
\end{aligned}$$

$$\begin{aligned}
v = u_g = u_{Ag} - |\mathbf{U}_a|D^{-1}[&(\cos\Theta\,\cos\Psi) \\
&+ \tan\beta\cdot(\sin\Phi\,\sin\Theta\,\cos\Psi - \cos\Phi\,\sin\Psi) + \tan\alpha(\cos\Phi\,\sin\Theta\,\cos\Psi + \sin\Phi\,\sin\Psi)],
\end{aligned}$$

$$w = -w_g = -w_{Ag} + |\mathbf{U}_a|D^{-1}[(-1\,\sin\Theta) + \tan\beta(\sin\Phi\,\cos\Theta) + \tan\alpha(\cos\Phi\,\cos\Theta)], \tag{5}$$

with inertial velocity vector $\mathbf{V}_g = (u_{Ag}, v_{Ag}, w_{Ag})$ and the Euler (attitude) angles' pitch Θ, true heading Ψ, and roll Φ.

4. Calibration of the airflow angles

The calibration of the 5HP was performed at the Pfleiderer Institute (TU Braunschweig), which provided an open wind tunnel capable of wind velocities up to 100 m s^{-1}. The 5HP was mounted on the M^{2}AV fuselage nose and was calibrated at an airflow velocity of 22 m s^{-1} and at predefined airflow angles $\tilde{\alpha}$ and $\tilde{\beta}$ between –20° and + 20° (with a $\Delta\tilde{\alpha}$ and $\Delta\tilde{\beta}$ of 2°). The measurement uncertainty of the wind tunnel velocity was 0.7% ($\approx$0.2 m s^{-1} for the specified velocity of 22 m s^{-1}). The airflow angles were varied manually during the calibration with an uncertainty of 0.2°.

These wind tunnel angles $\tilde{\alpha}$ and $\tilde{\beta}$ are related to the airflow angles α and β (Boiffier 1998) used for the wind calculation (5):

$$\alpha = \tilde{\alpha},$$

$$\beta = \arctan\left(\frac{\tan\tilde{\beta}}{\cos\tilde{\alpha}}\right). \tag{6}$$

The 5HP has five total pressure ports on its conical head and four static pressure ports downstream of the head (Fig. 2). Five differential pressures are measured: the difference between the central hole and each of the four remaining total pressure ports (ΔP_{01}, ΔP_{02}, ΔP_{03}, ΔP_{04}) and the difference between the static pressure and the central hole (ΔP_{0s}). These measurements are used to determine a total pressure difference (Sasongko 1997):

$$\Delta P = \left[\frac{1}{5}\sum_{i=0}^{4}\left(P_i - \frac{1}{5}\sum_{j=0}^{4}P_j\right)^2\right]^{1/2} + \left[P_0 - \frac{1}{4}\sum_{i=1}^{4}P_i\right], \tag{7}$$

which uses the absolute pressures $P_0 \ldots P_4$. Equation (7) can be rewritten by using the differential pressure measurements $\Delta P_{01} \ldots \Delta P_{04}$:

$$\Delta P = \left\{\frac{1}{125}[(\Delta P_{01} + \Delta P_{02} + \Delta P_{03} + \Delta P_{04})^2 + (-4\Delta P_{01} + \Delta P_{02} + \Delta P_{03} + \Delta P_{04})^2 + (\Delta P_{01} - 4\Delta P_{02} + \Delta P_{03} + \Delta P_{04})^2 + (\Delta P_{01} + \Delta P_{02} - 4\Delta P_{03} + \Delta P_{04})^2 + (\Delta P_{01} + \Delta P_{02} + \Delta P_{03} - 4\Delta P_{04})^2]\right\}^{(1/2)} + \frac{1}{4}(\Delta P_{01} + \Delta P_{02} + \Delta P_{03} + \Delta P_{04}). \tag{8}$$

The dimensionless pressure coefficients k_α and k_β are defined using ΔP and the measured differential pressures

$$k_\alpha = \frac{\Delta P_{01} - \Delta P_{03}}{\Delta P} \quad \text{and} \tag{9}$$

$$k_\beta = \frac{\Delta P_{02} - \Delta P_{04}}{\Delta P}. \tag{10}$$

To calculate the airflow angles and the dimensionless coefficient k_q for the dynamic pressure, three functions were defined:

$$\tilde{\alpha} = f_1(k_\alpha, k_\beta),$$

$$\tilde{\beta} = f_2(k_\alpha, k_\beta), \quad \text{and}$$

$$k_q = f_3(k_\alpha, k_\beta), \tag{11}$$

with the general calibration polynomial form (11th order) for f_x (x = 1, 2, or 3) according to Bohn and Simon (1975)

$$f_x(k_\alpha, k_\beta) = \sum_{i=0}^{m}(k_\alpha)^i[\sum_{j=0}^{n}X_{ij}(k_\beta)^j], \tag{12}$$

where $m = n = 11$ and X_{ij} represents the coefficients for the angle of attack a_{ij}, the sideslip angle b_{ij}, or the dynamic pressure q_{ij} for f_1, f_2, and f_3 respectively. The function (12) contains $m \cdot n$ unknown coefficients which can be determined with a system of $m \cdot n$ independent equations. This linear problem is solved by the least squares method for all three functions (11) and returns the coefficients a_{ij}, b_{ij}, and q_{ij}.

The method enables the determination of the airflow angles and the dynamic pressure coefficient k_q with the measurements of the 5HP. Finally the dynamic pressure q during flight is calculated

$$q = \Delta P_{0s} + \Delta P k_q \tag{13}$$

and used to calculate the true airspeed (4).

5. Determination of the attitude angles

The reliable determination of the attitude, velocity, and position of the aircraft is essential for wind identi-

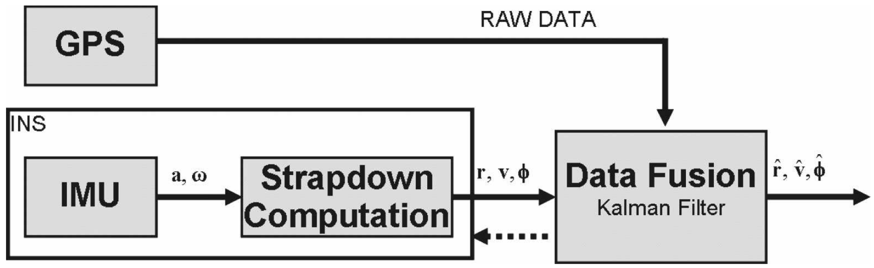

FIG. 4. Navigation filter structure, where **a** and ω are the acceleration and angular rate from the IMU and **r, v**, and ϕ are the position, velocity, and attitude from the INS system. The position, velocity, and attitude solution from the Kalman filter are defined as $\hat{\mathbf{r}}$, $\hat{\mathbf{v}}$, and $\hat{\phi}$.

fication. With the M^{2}AV this is achieved by an integrated navigation system consisting of a GPS and an INS. The INS calculates the position, velocity, and attitude by a strapdown calculation of the accelerations and angular rates measured by the IMU. The GPS–INS system offers a significantly increased performance, compared to an INS only, due to the complementary characteristics of GPS and INS; the latter assures the continuous availability of the attitude, velocity, and position. The growth of navigation errors with time due to the low-cost MEMS IMU is prevented by the use of aiding information provided by the GPS receiver. Figure 4 displays the navigation-filter architecture.

For the GPS–INS integration a discrete error state Kalman filter was used (Gelb 1989). Kalman filters are based on linear dynamic systems discretized in the time domain (Kálmán 1960). The system model uses the following discrete error-state vectors: three position errors, three velocity errors, and three attitude errors, as well as three errors in the gyro sensor signal bias, three errors in the accelerometer signal bias, one error in the GPS receiver clock, and one error in the clock drift, which are in total 17 states. By processing GPS raw data (pseudo range, delta range, and carrier phase), estimates of the error-state vector are made to correct the full states of the navigation system. The GPS receiver measures the delay of the satellite signal and calculates the distance to the satellite, which is called the pseudo range. The delta range is the velocity of the GPS receiver relative to the satellite calculated via Doppler shift of the carrier wave. The receiver gives also the phasing of the carrier wave. This method of aiding is called tightly coupled (Wendel and Trommer 2004). Furthermore, with such a filter the INS can still be aided by GPS when there are less than four visible satellites. A tightly coupled GPS–INS filter usually processes pseudo ranges and delta ranges. Based on the method used by Farrell (2001) and van Graas and Farrell (2001), the delta ranges can be replaced by time-differenced carrier phases and used for the M^{2}AV navigation (Winkler and Vörsmann 2007). It was proven that the filter with a time-differenced carrier phase achieved a better velocity and attitude accuracy than the filter using delta ranges. The method allows using the high measurement accuracy of the carrier phase without solving the integer ambiguities. Compared to a delayed-state Kalman filter (which would be commonly used in such case), this method does not induce additional cross-correlation between measurements at one epoch.

a. *Observability*

The Kalman filter can be used to determine the state of the system that is not directly measured. In this case, the Kalman filter will operate as an observer. A system is observable when the states can be identified by the measurements (GPS raw data).

The performance of the GPS–INS system depends on the M^{2}AV maneuvers. More precisely, the flight dynamic is responsible for the observability and hence for the attitude, velocity, and position estimation quality. The following relations were defined from the observability matrix (described in detail by Winkler and Vörsmann 2007), assuming that the body coordinate system equals the geodetic system (Euler angles Ψ, Φ, and $\Theta = 0$):

$$
\begin{aligned}
c_x &= -a_y\delta\Psi + a_z\delta\Theta + \delta a_x,\\
c_y &= a_x\delta\Psi - a_z\delta\Phi + \delta a_y, \quad \text{and}\\
c_z &= a_y\delta\Phi - a_x\delta\Theta + \delta a_z,
\end{aligned}
\tag{14}
$$

where c_x, c_y, and c_z represent the acceleration errors (in the x, y, and z directions, respectively, in the geodetic or body coordinate system) provided by the GPS. Using an error-state filter, the system errors are determined; from these, the full-state navigation solution can also be solved (like the attitude, velocity, and position). Because the unknown error angles $\delta\Phi$, $\delta\Theta$, and $\delta\Psi$ (roll, pitch, and true heading) are assumed to be small, these

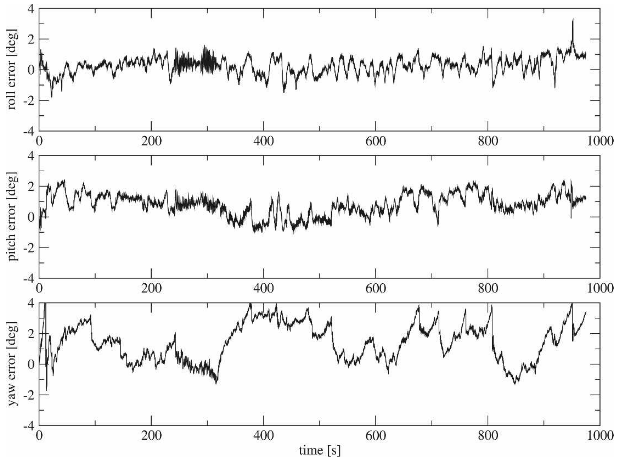

FIG. 5. Roll, pitch, and yaw (true heading) errors, determined during the test flight of 17 May 2006, with the FOG IMU reference system.

were approximated from trigonometric functions. The parameters a_x, a_y, and a_z are the acceleration in x, y, and z direction, and δa_x, δa_y, and δa_z are the corresponding accelerometer bias-errors determined by the Kalman filter.

During flight, the horizontal accelerations are smaller than the vertical accelerations because of gravity. If the horizontal acceleration is neglected ($a_x \ll a_z$ and $a_y \ll a_z$), (14) can be reduced to

$$\begin{aligned} c_x &= a_z \delta\Theta + \delta a_x, \\ c_y &= -a_z \delta\Phi + \delta a_y, \quad \text{and} \\ c_z &= \delta a_z, \end{aligned} \tag{15}$$

where $\delta\Theta$, $\delta\Phi$, δa_x, δa_y, and δa_z are the remaining unknown parameters.

The pitch angle can only be observed in combination with δa_x and the roll angle can only be observed in combination with δa_y (15). The heading observation results from two combinations (14): first, the combination of the pitch angle, δa_x, and the heading and second, the roll angle, δa_y, and the heading. Thus, the true heading cannot be observed directly. The heading estimation is always a combination of respective filter states and thus the heading varies in its dependency on the estimation. The variability of the heading can be seen in Fig. 5. A more detailed discussion and an extensive observability analysis of the GPS–INS system based on the observability matrix are provided by Winkler and Vörsmann (2007).

The test flight described here was performed under ideal flight conditions: highly dynamical flight with continuous change of flight maneuvers. The observability of the Euler angles is best when the M^{2}AV experiences accelerations in the x, y, and z directions.

For the extreme case of a steady cruising flight in a stationary nonturbulent flow with no significant horizontal accelerations, (15) shows that the absence of these accelerations results in a loss of the heading correction. So, a rotation about the vertical axis, which equals a heading change, has no effect on the velocity vector during this phase. The only observational information provided by GPS is position and velocity. During this flight phase, the heading is supported by INS only, which means that the heading is the integration of the vertical gyro and its error. Thus, the heading remains uncorrected and drifts conditionally on the gyro error during a flight without horizontal accelerations.

However, during a flight in the atmospheric boundary layer, horizontal accelerations always occur because of atmospheric turbulence. The larger these horizontal accelerations, the better the true heading can be observed and corrected. From practical experience, a compromise was found between the needs for, on the one hand, a long steady flight to achieve small statistical meteorological measurement errors and, on the other, a highly dynamic flight to obtain the optimal filter observability. Flights in the convective boundary layer with straight and level legs up to 6 km include enough horizontal acceleration for an adequate heading determination. Shorter flight legs (2 km) in the stable boundary layer are recommended to achieve sufficient dynamics in the turns.

The M^{2}AV wind measurement unit is still under development. It is planned to improve the navigation solution from the Kalman filter by the implementation of a magnetic compass, in addition to the INS–GPS. A reduction of the variable error and drift of the true heading will result in a more accurate determination of the horizontal wind components.

b. *Flight test*

A flight test was carried out on 17 May 2006 near Braunschweig with a duration of 16 min to identify the achievable accuracy of the navigation solution under realistic conditions. The M^{2}AVwas additionally equipped with a navigation reference system based on a fiber optical gyro (FOG) IMU with an attitude accuracy of approximately 0.01° and a velocity accuracy of approximately 0.05 m s^{-1}. The M^{2}AV low-cost GPS–MEMS–IMU was compared to this reference system. Figure 5 shows the angle errors that resulted from the differences between the systems. The characteristics of the roll and pitch errors are representative for the velocity errors (not plotted here). The accuracy achieved during the flight is summarized in Table 3. The largest

TABLE 3. Kalman filter: attitude and velocity accuracy (σ) achieved during the flight with the reference IMU (17 May 2006).

Roll angle	0.54°
Pitch angle	0.71°
Yaw angle	1.22°
Velocity north	0.18 m s^{-1}
Velocity east	0.16 m s^{-1}
Velocity down	0.58 m s^{-1}

error occurred for the true heading (or yaw angle), which is usually the most difficult angle to determine in flight.

6. Wind vector calibration

The wind vector (5) calculated from airborne measurements is very sensitive to errors in the input parameters. The first M^{2}AV datasets were measured in both convective and neutral stratification. During these flights, the mean vertical wind was expected to be nearly zero, but the actually measured $\overline{w}$ showed a deviation of a few meters per second. The mean horizontal wind components were assumed to be constant during the entire flight. However, both the measured u and v time series showed offsets depending on the flight direction compared to $\overline{u}$ and $\overline{v}$ for a complete square-shaped pattern.

a. *The impact of sensor errors on the wind calculation*

A simple error estimation (Vörsmann 1985) was made to identify the parameters causing the above-described systematic errors in the horizontal and vertical wind components. To quantify the errors, a reference state for the M^{2}AV was defined (Table 4): a typical airspeed of 20 m s^{-1}, small airflow angles and Euler angles (0.02 rad), and a vertical velocity of 1 m s^{-1}; the horizontal velocity components were set to 20 m s^{-1} depending on the flight direction. The reference wind components (u_{ref}, v_{ref}, and w_{ref}) were calculated as a function of the true heading (0 . . . 360°).

The effect of every individual parameter (nine parameters in total) was determined by defining typical measurement errors with values of 0.5 m s^{-1} for the velocities and 0.02 rad ($\approx$1°) for the angles. These errors were added to the reference states and used to determine the individual contributions to each component (u_{err}, v_{err}, and w_{err}) of the calculated wind vector (see Table 4).

Except for the inertial velocity components, the error estimations for u and v depended on the flight direction (Table 4). An error in the sideslip angle or the true heading resulted in an erroneous u component in the north (0°) or south (180°) flight direction and an erroneous v component in east (90°) or west (270°) flight direction. A true airspeed error also affected both u and v significantly depending on the flight direction. The largest deviation of w was caused by the errors in Θ, α, and the vertical velocity w_{Ag}, independent of the flight direction, as expected.

Assuming that the separation of the IMU origin and the 5HP is negligible, the true airspeed measured by the 5HP is transformed into the IMU coordinate system (defined as the body coordinate system) by the angles $\Delta\Phi'$, $\Delta\Theta'$, and $\Delta\Psi'$, corresponding to rotations about the x, y, and z axes, respectively. These angles are unknown and represent the mechanical misalignment between the 5HP and the IMU (which should be the in the same coordinate system in the ideal case). To transform the measured true airspeed into geodetic coordinates, the Euler angles (measured by the INS–GPS) are increased by these unknown angles $\Delta\Phi'$, $\Delta\Psi'$, and $\Delta\Theta'$. As shown by the error estimation, the error in Φ had an insignificant effect on the computed u, v, and w; therefore, $\Delta\Phi'$ was neglected and set to zero. Although the remaining biases cannot be measured, a flight strategy was chosen to determine $\Delta\Theta'$ and $\Delta\Psi'$.

The dynamic pressure (and the true airspeed) was calculated using the wind tunnel calibration polynomi-

TABLE 4. Error estimation: differences Δu, Δv, and Δw between the reference and erroneous wind components.

Parameter	Typical value	Δu	Δv	Δw
Ψ	$0 \ldots 2\pi$ rad	$0.4 \cos \Psi$	$-0.4 \sin \Psi$	0
Θ	0.02 rad	$-4 \times 10^{-3} \sin \Psi$	$-4 \times 10^{-3} \cos \Psi$	-0.4
Φ	0.02 rad	$-8 \times 10^{-3} \cos \Psi$	$-8 \times 10^{-3} \sin \Psi$	-8×10^{-5}
α	0.02 rad	$-4 \times 10^{-3} \sin \Psi$	$-4 \times 10^{-3} \cos \Psi$	0.4
β	0.02 rad	$0.4 \cos \Psi$	$-0.4 \sin \Psi$	0
$\mathbf{U}_a$	20 m s^{-1}	$0.5 \sin \Psi$	$0.5 \cos \Psi$	0
v_{Ag}	$20 \times \sin \Psi$ m s^{-1}	-0.5	0	0
u_{Ag}	$20 \times \cos \Psi$ m s^{-1}	0	-0.5	0
w_{Ag}	1 m s^{-1}	0	0	-0.5

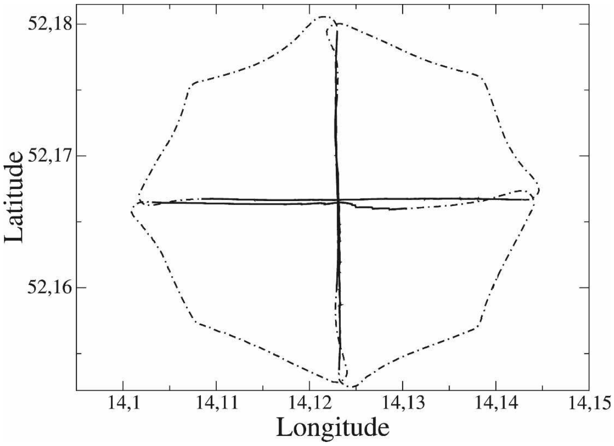

FIG. 6. Star flight pattern performed on 1 Aug 2007. The dashed–dotted line represents the complete flight; the solid lines show the horizontal legs used for the in-flight calibration.

als. Unfortunately, the wind tunnel was too small for the complete aircraft and therefore the calibration setup was reduced to a shorter fuselage. The wing of the aircraft, including both engines and the full body, was not taken into account and therefore the actual flow distortion during flight was not included in the calibration. This effect can only be corrected by a new calibration in a larger wind tunnel or by an in-flight calibration. Because a new calibration in a larger wind tunnel is currently not feasible, the aerodynamic effect of the wings and the propulsion is approximated by a correction factor $f_{\mathbf{U}_a}$ of the true airspeed.

b. In-flight wind calibration

In total three angles—$\Delta\Psi'$, $\Delta\Theta'$, and $f_{\mathbf{U}_a}$—have to be determined. The appropriate flight pattern for the in-flight calibration is a star pattern (Fig. 6). The ideal atmospheric conditions for the in-flight calibration are no large turbulent transport, a constant mean horizontal wind, and a mean vertical wind near zero. For every straight horizontal leg, the mean values ($\overline{\mathbf{U}}_a$, $\overline{\alpha}$, $\overline{\beta}$, $\overline{\Theta}$, $\overline{\Psi}$, $\overline{\Phi}$, $\overline{u}_{Ag}$, $\overline{v}_{Ag}$, and $\overline{w}_{Ag}$, uncorrected) will be calculated from the measured time series. These mean values will be used to calculate the mean wind vector using Eq. (5), which is supplemented by the unknown correction factors. The following parameters are replaced in (5):

$$\Theta \Rightarrow \overline{\Theta} + \Delta\Theta',$$
$$\Psi \Rightarrow \overline{\Psi} + \Delta\Psi', \quad \text{and}$$
$$\mathbf{U}_a \Rightarrow \overline{\mathbf{U}}_a f_{\mathbf{U}_a}, \tag{16}$$

where $\overline{\Theta}$, $\overline{\Psi}$, and $\overline{\mathbf{U}}_a$ are the mean values of the pitch angle, true heading, and true air speed, respectively.

The assumptions that the mean horizontal wind components are actually identical on a round trip (two identical legs flown in reverse direction) and that the mean vertical wind is close to zero lead to the following set of equations:

$$\overline{u}^n - \overline{u}^s = 0, \quad \overline{v}^n - \overline{v}^s = 0,$$
$$\overline{u}^w - \overline{u}^e = 0, \quad \overline{v}^w - \overline{v}^e = 0, \quad \text{and}$$
$$\overline{w}^n = \overline{w}^s = \overline{w}^w = \overline{w}^e = 0, \tag{17}$$

where n, s, w, and e indicate north, south, west, or east flight direction.

The unknown angles $\Delta\Psi'$, $\Delta\Theta'$, and f_{U_a} are calculated from (17) where u, v, and w are calculated by (5) using the substitutions from (16). The Levenberg–Marquardt least squares fit method (Press et al. 1992) is used to solve the equations.

c. Experimental setup

A field campaign was carried out in the beginning of August 2007 near the boundary layer measurement field of the DWD, located 5 km south of the Meteorological Observatory Lindenberg, near Falkenberg. The lower part of the boundary layer was probed by a 99-m tower, a 12-m tower, and a combined sodar and radio acoustic sounding system (RASS). A large-aperture scintillometer (LAS) was installed over a path length of 4.7 km. The LAS transmitter was installed at the 99-m tower in Falkenberg and the receiver on a 30-m lattice tower at the MOL observatory site.

The main goal at the experiment was the comparison of the M^2AV wind measurements with tower and sodar measurements. The 99-m tower provided measurements of temperature, humidity, and wind speed at four levels (40, 60, 80, and 98 m). The wind direction was measured at heights of 40 and 98 m only. The sodar wind speed and wind direction profiles reached from 5 to 350 m above ground. Tower and sodar measurements were available for all the flight periods during the campaign.

During the 2-day experiment, six M^2AV flights were performed. A special calibration flight was performed at 1850–1920 UTC 1 August 2007, with two star patterns at 280 m above ground. During this calibration flight, a vertical wind component close to zero, weak turbulence, a constant mean horizontal wind, and low wind speed (less than 5 m s^{-1}) were observed. During daytime in moderate convection, two 3D box patterns, Fig. 7, were flown, which consisted of several square-shaped patterns (four legs) flown around the 99-m tower at different heights. Seven square patterns (with flight legs of 650 m) at four flight levels (170, 113, 90,

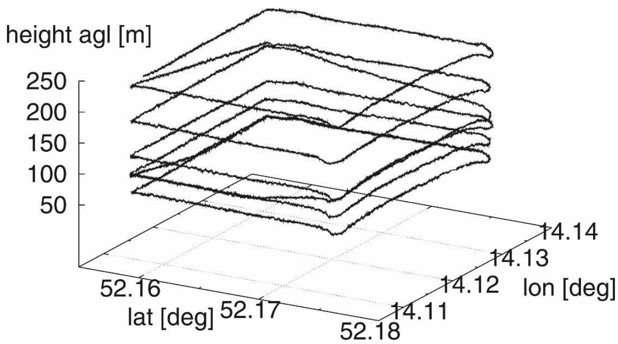

FIG. 7. The flight track of the 3D box pattern flown on 2 Aug 2007.

and 68 m) were flown during the first 3D box. The second 3D box consisted of five square patterns (with leg lengths of 1600 m) at five different heights (230, 173, 115, 87, and 58 m). Because the 3D box flights give information on the mean vertical structure of the boundary layer, these measurements were compared with the 99-m tower and sodar profiles.

7. Results

a. Calibration flight

The in-flight calibration method was applied on the measurements of the calibration flight (1 August 2007). The following correction factors were determined:

(i) the correction for the pitch angle, $\Delta\Theta' = -1.0°$,
(ii) the correction factor for TAS, $f_{\mathbf{U}_a} = 1.04$, and
(iii) it was not possible to determine a constant correction for the true heading.

The calculated correction factors $\Delta\Psi'$ for both star patterns differed significantly. The results from previous calibration flights (performed near Braunschweig) also showed diverse $\Delta\Psi'$ estimations for each flight day and even flight level. Obviously, $\Delta\Psi'$ included not only the constant mechanic misalignment between the IMU and 5HP but also the variable error of Ψ calculated by the Kalman filter. As discussed before, the calculation of Ψ is complex and significant (variable) errors can occur because of the filter properties.

To define this variable Ψ error, the calibration method was also applied to suitable box and star flights under moderate convective conditions, which consist of four legs oriented in the north, south, west, and east directions. For each flight the $\Delta\Psi'$ was calculated. Together with the already calculated $\Delta\Theta'$ (−1.0) and $f_{\mathbf{U}_a}$ (1.043), the time series of the horizontal and vertical wind were calculated.

b. Wind measurements

The power spectra of the time series of u, v, and w showed no systematic errors or noise (Fig. 8). All three spectra exhibit an $f^{-5/3}$ law of the inertial subrange of

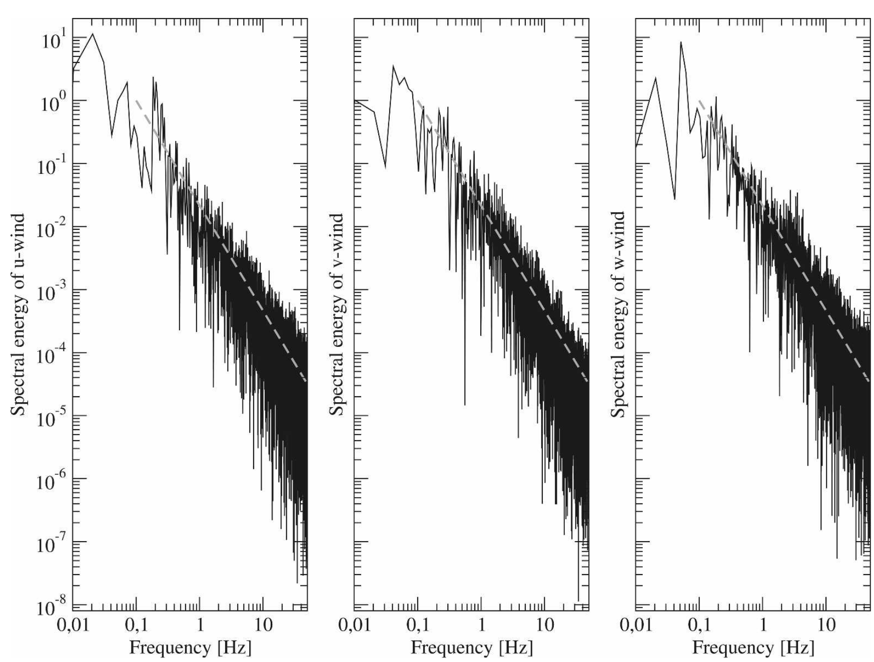

FIG. 8. Example of the variance spectra of the u, v, and w wind components, measured by the M^2AV on 2 Aug 2007. The gray dashed line represents the $f^{-5/3}$ law.

TABLE 5. Results from both 3D box patterns flown around the 99-m tower. The horizontal wind speed U_{hor} and the wind direction Ω_{hor} are listed for every box; σ represents the std dev of the measurements. The sodar and tower measurements are written in the same row as the compared M^{2}AV data.

	M^{2}AV			Sodar			99-m tower		
Flight/leg	z (m)	U_{hor} (σ) (m s^{-1})	Ω_{hor} (σ) (°)	z (m)	U_{hor} (m s^{-1})	Ω_{hor} (°)	z (m)	U_{hor} (m s^{-1})	Ω_{hor} (°)
1/01	168	3.53 (0.74)	242 (21)	160	3.7	246			
1/02	168	3.74 (0.52)	242 (10)	180	3.5	224			
1/03	112	3.41 (0.21)	241 (11)	120	3.6	238	98	3.7	255
1/04	111	3.65 (0.50)	251 (8)	120	3.6	238	98	3.7	255
1/05	89	3.58 (0.46)	259 (8)	80	3.3	237	80	2.9	
1/06	67	3.17 (0.77)	233 (12)	60	3.4	264	60	2.8	
1/07	67	3.14 (0.76)	234 (8)	80	3.5	217	60	3.4	
1/07							40	3.2	237
2/01	228	6.70 (0.47)	151 (13)	220	5.1	151			
2/01				240	5.5	149			
2/02	171	6.20 (0.07)	152 (6)	160	4.5	142			
2/02				180	5.3	142			
2/03	114	5.75 (0.77)	141 (5)	100	5.8	152	98	6.2	144
2/04	86	6.04 (0.08)	148 (5)	80	5.7	143	80	5.6	
2/05	58	6.91 (0.76)	159 (5)	60	4.8	156	60	5.8	
2/05							40	5.5	150

isotropic turbulence up to 40 Hz, which corresponds to a spatial resolution of 0.55 m (at 22 m s^{-1} airspeed).

The mean wind components were calculated for each square-shaped pattern at a certain altitude (see Table 5). For each M^{2}AV flight level, the corresponding tower (10-min average) and sodar (15-min average) measurements at about the same height were selected (Table 5; Figs. 9 and 10). On the first flight (Fig. 9) the horizontal wind was weak (3–4 m s^{-1}). The M^{2}AV mean horizontal wind speed agreed well within the statistical error bars (1 m s^{-1}) with both sodar and tower measurements.

Because of the low wind speed, the wind direction strongly fluctuated within 60° over the entire measured height (see sodar data, Fig. 9), covering the averaged M^{2}AV measurements (which were compromised by a 20° error bar). A stronger wind speed was observed by all involved systems on the second day (Fig. 10), which resulted in smaller fluctuation in the wind direction. During this flight, the M^{2}AV measured a somewhat larger mean wind speed compared to the sodar but agreed with the tower measurements. The airborne-measured mean wind direction agreed well with both sodar and tower data, with smaller statistical uncertainties compared to the first flight.

Measurements of the mean vertical wind with airborne systems are usually quite inaccurate. It was no surprise that the mean vertical wind measured by the M^{2}AV was accompanied by large standard deviations up to 0.4 m s^{-1} (Fig. 11 and Table 6). Nevertheless, the

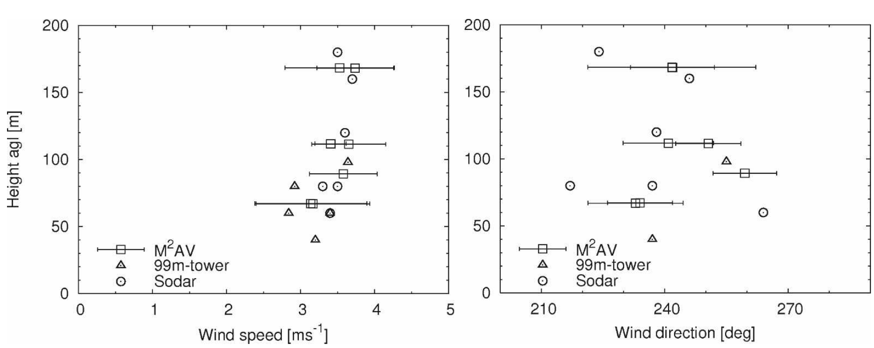

FIG. 9. Wind speed and wind direction for the first 3D box flight performed between 0922 and 0952 UTC 1 Aug 2007. The M^{2}AV data at the same height were measured during two consecutive square-shaped flight patterns. The error bars represent the std devs of the M^{2}AV measurements (Table 5). For every M^{2}AV time interval and height the corresponding tower (10-min average) and sodar (15-min average) measurements were plotted.

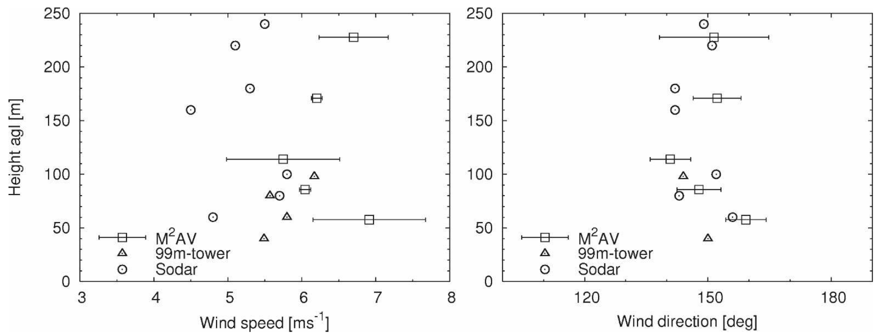

FIG. 10. Wind speed and wind direction measured between 0837 and 0915 UTC 2 Aug 2007. The error bars represent the std devs of the M^{2}AV measurements (Table 5).

vertical wind measurements on both flight days agreed with the sodar measurements within their statistical uncertainty.

8. Conclusions

The M^{2}AV was developed as a low-cost and easy-to-handle system for boundary layer research that is not remotely controlled by a pilot on the ground but rather operates autonomously. The advantages of the autopilot are the possibilities of flying out of sight (long distance flights) or at night (stable boundary layer research). At a typical airspeed of 22 m s^{-1} the M^{2}AV can reach a flight distance of 60–70 km. It was not intended to compete with large and heavy airborne research systems (e.g., the Helipod; Bange and Roth 1999) in terms of data accuracy. Nevertheless, the results are quite promising because the systematic measurement errors (mainly caused by the use of light, small, and inexpensive sensors) are acceptably small. The temporal (and thus spatial) resolution of the wind measurement is remarkably high. Power spectra exhibit an $f^{-5/3}$ law of the inertial subrange of isotropic turbulence up to 40 Hz (or 0.55 m at 22 m s^{-1} airspeed). There are only a few research aircraft that are able to resolve submeter turbulence, mainly due to the disturbance of the atmospheric flow by large fuselages, engines, and wings.

An in-flight calibration method was developed to correct the measured wind with a constant correction factor for the true airspeed (only 1.04, presumably due to the reduced wind tunnel settings) and correction angles $\Delta\Theta'$ and $\Delta\Psi'$. The determined $\Delta\Theta'$ represents the construction misalignment between the 5HP and the IMU by a rotation on the y axis (in the body coordinate system). The error in Ψ was caused not only by a constant mechanic misalignment; it also included a variable error due to Kalman filter properties, causing a variable $\Delta\Theta'$. To correct for this error, the in-flight calibration had to be applied on every (square-shaped or star) flight pattern, assuming a homogeneous wind field. The wind vector was recalculated using the correction factors and compared with sodar and tower measurements during a 2-day field experiment. Despite the short averaging length of the M^{2}AV data in the convective boundary layer, the measurements agreed with the tower and sodar data. Particular for the first flight with weak wind conditions, the mean wind speed agreed with the sodar and tower data within 1 m s^{-1}. In

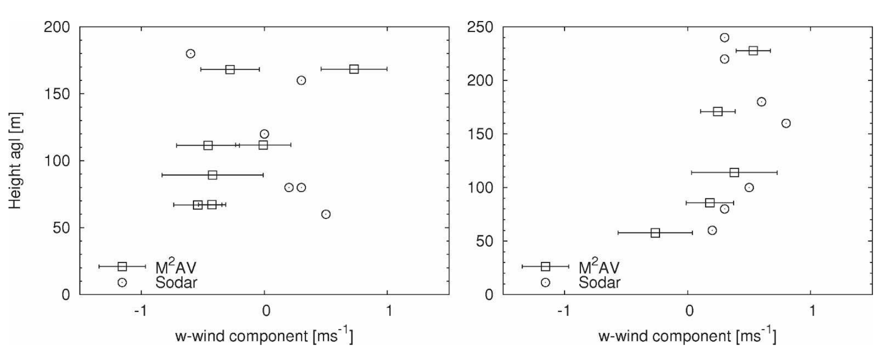

FIG. 11. Vertical wind; the error bars represent the std devs of the M^{2}AV measurements (Table 6). (left) First 3D box flight, 1 Aug; (right) second 3D box flight, 2 Aug.

TABLE 6. Results from both 3D box patterns flown around the 99-m tower. The vertical wind speed w and the std dev σ are listed for every box. The sodar measurements are written in the same row as the compared M^{2}AV data.

	M^{2}AV		Sodar	
Flight/leg	z (m)	w (σ) (m s^{-1})	z (m)	w (m s^{-1})
1/01	168	0.7 (0.3)	160	0.3
1/02	168	−0.3 (0.2)	180	−0.6
1/03	112	−0.0 (0.2)	120	0.0
1/04	111	−0.5 (0.3)	120	0.0
1/05	89	−0.4 (0.4)	80	0.2
1/06	67	−0.5 (0.2)	60	0.5
1/07	67	−0.4 (0.1)	80	0.3
2/01	228	0.5 (0.1)	220	0.3
2/01			240	0.3
2/02	171	0.2 (0.1)	160	0.8
2/02			180	0.6
2/03	114	0.4 (0.4)	100	0.5
2/04	86	0.2 (0.2)	80	0.3
2/05	58	−0.3 (0.3)	60	0.2

stronger wind, the M^{2}AV measured higher mean wind speeds compared to the sodar profiles but agreed with the tower measurements.

Acknowledgments. We are much obliged to Frank Beyrich of the Meteorological Observatory Lindenberg, who gave us the opportunity to perform measurement flights at the MOL site and provided the corresponding sodar, tower, and LAS data. We would also like to thank Daniel Nerger of the Institute of Fluid Mechanics (TU Braunschweig) for his support concerning the wind tunnel calibration and for providing the calculated wind tunnel calibration coefficients. The data analysis is funded by the German Science Foundation DFG (FSA: Fine Structure of the Stably Stratified Atmospheric Boundary Layer in Antarctica, within "Schwerpunktprogramm 1158 Antarktisforschung", Grant Ba 1988/4–1).

REFERENCES

Axford, D. N., 1968: On the accuracy of wind measurements using an inertial platform in an aircraft, and an example of a measurement of the vertical mesostructure of the atmosphere. *J. Appl. Meteor.,* **7,** 645–666.

Bange, J., and R. Roth, 1999: Helicopter-borne flux measurements in the nocturnal boundary layer over land—A case study. *Bound.-Layer Meteor.,* **92,** 295–325.

——, F. Beyrich, and D. A. M. Engelbart, 2002: Airborne measurements of turbulent fluxes during LITFASS-98: A case study about method and significance. *Theor. Appl. Climatol.,* **73,** 35–51.

Beyrich, F., and H.-T. Mengelkamp, 2006: Evaporation over a heterogeneous land surface: EVA_GRIPS and the LITFASS-2003 experiment—An overview. *Bound.-Layer Meteor.,* **121,** 5–32.

Bohn, D., and H. Simon, 1975: Mehrparametrige approximation der Eichraume und Eichflächen von Unterschall- bzw. Uberschall-5-Loch-Sonden. Archiv fur Technisches Messen and Meßtechnische Praxis Vol. 470 (3), 31–37.

Boiffier, J.-L., 1998: *The Dynamics of Flight*: *The Equations*. Wiley, 353 pp.

Brown, E. N., C. A. Friehe, and D. H. Lenschow, 1983: The use of pressure fluctuations on the nose of an aircraft for measuring air motion. *J. Appl. Meteor.,* **22,** 171–180.

Buschmann, M., J. Bange, and P. Vörsmann, 2004: MMAV—A miniature unmanned aerial vehicle (mini-UAV) for meteorological purposes. Preprints, *16th Symp. on Boundary Layers and Turbulence,* Portland, ME, Amer. Meteor. Soc., 6.7. [Available online at http://ams.confex.com/ams/pdfpapers/77875.pdf.]

——, A. Heindorf, S. Winkler, and P. Vörsmann, 2006: MINC: A miniature integrated guidance, navigation and control system enables in-flight GPS/INS data fusion aboard a micro aerial vehicle. *Proc. 25th Congress of the Int. Council of the Aeronautical Sciences,* Hamburg, Germany, ICAS.

Crawford, T. L., and R. J. Dobosy, 1992: A sensitive fast-response probe to measure turbulence and heat flux from any airplane. *Bound.-Layer Meteor.,* **59,** 257–278.

Egger, J., and Coauthors, 2002: Diurnal winds in the Himalayan Kali Gandaki Valley. Part III: Remotely piloted aircraft soundings. *Mon. Wea. Rev.,* **130,** 2042–2058.

Farrell, J. L., 2001: Carrier phase processing without integers. *Proc. ION 57th Annual Meeting,* Albuquerque, NM, Institute of Navigation, 423–428.

Gelb, A. H., Ed., 1989: *Applied Optimal Estimation*. MIT Press, 374 pp.

Grossman, R. L., 1977: A procedure for the correction of biases in winds measured from aircraft. *J. Appl. Meteor.,* **16,** 654–658.

Haering, E. A., 1990: Airdata calibration of a high-performance aircraft for measuring atmospheric wind profiles. NASA Tech. Memo. 101774, 24 pp.

Hobbs, S., D. Dyer, D. Courault, A. Olioso, J.-P. Lagouarde, Y. Kerr, J. McAneney, and J. Bonnefond, 2002: Surface layer profiles of air temperature and humidity measured from unmanned aircraft. *Agron. J.,* **22,** 635–640.

Holland, G. J., and Coauthors, 2001: The aerosonde robotic aircraft: A new paradigm for environmental observations. *Bull. Amer. Meteor. Soc.,* **82,** 889–901.

Kálmán, R. E., 1960: A new approach to linear filtering and prediction problems. *Trans. AMSE, J. Basic Eng.,* **82D,** 35–45.

Khelif, D., S. P. Burns, and C. A. Friehe, 1999: Improved wind measurements on research aircraft. *J. Atmos. Oceanic Technol.,* **16,** 860–875.

Leach, B. W., and J. I. MacPherson, 1991: An application of Kalman filtering to airborne wind measurements. *J. Atmos. Oceanic Technol.,* **8,** 51–65.

Leise, J. A., and J. M. Masters, 1993: Wind measurements from aircraft. U.S. Department of Commerce, National Oceanic and Atmospheric Administration, Aircraft Operation Center, 166 pp.

Lenschow, D. E., 1986: *Probing the Atmospheric Boundary Layer.* Amer. Meteor. Soc., 269 pp.

Ma, S., H. Chen, G. Wang, Y. Pan, and Q. Li, 2004: A miniature robotic plane meteorological sounding system. *Adv. Atmos. Sci.,* **21,** 890–896.

Press, W., B. Flannery, S. Teukolsky, and W. Vetterling, 1992: *Numerical Recipes in C: The Art of Scientific Computing.* 2nd ed. Cambridge University Press, 994 pp.

Sasongko, H., 1997: *Rand- und Spaltströmungen in Stark Gestaffelten Verdichtergittern aus Schwach Gewölbten Profilen.* Technische Universität Braunschweig, 167 pp.

Scott, S. G., T. P. Bui, K. R. Chan, and S. W. Bowen, 1990: The meteorological measurement system on the NASA ER-2 aircraft. *J. Atmos. Oceanic Technol.,* **7,** 525–540.

Soddell, J. R., K. McGuffie, and G. J. Holland, 2004: Intercomparison of atmospheric soundings from the aerosonde and radiosonde. *J. Appl. Meteor.,* **43,** 1260–1269.

Spieß, T., J. Bange, M. Buschmann, and P. Vörsmann, 2007: First application of the meteorological mini-UAV "M^2AV." *Meteor. Z.,* **16,** 159–169.

Tjernström, M., and C. A. Friehe, 1991: Analyses of radome air-motion system on a twin-jet aircraft for boundary-layer research. *J. Atmos. Oceanic Technol.,* **8,** 19–40.

Van Graas, F., and J. L. Farrell, 2001: GPS/INS—A very different way. *Proc. ION 57th Annual Meeting,* Albuquerque, NM, Institute of Navigation, 715–721.

Vörsmann, P., 1985: Ein Beitrag zur bordautonomen Windmessung. Ph.D. dissertation, Technische Universität Braunschweig, 117 pp.

Wendel, J., and G. F. Trommer, 2004: Tightly coupled GPS/INS integration for missile applications. *Aerosp. Sci. Technol.,* **8,** 627–634.

Winkler, S., and P. Vörsmann, 2007: Multi-sensor data fusion for small autonomous unmanned aircraft. *Eur. J. Navig.,* **5,** 32–41.

Wood, R., I. M. Stromberg, P. R. Jonas, and C. S. Mill, 1997: Analysis of an air motion system on a light aircraft for boundary layer research. *J. Atmos. Oceanic Technol.,* **14,** 960–968.